Chapter 4 Chemical Solution Deposition of Zn$_{(1-x)}$Zr$_x$O Thin Films as Active Channel Layers of Thin Film Transistors

4.0 Preface

Sol-gel derived Zn$_{(1-x)}$Zr$_x$O films and thin film transistors (TFTs) were investigated in this study, where x ranging from 0.00 to 0.10. The effects of Zr additive on the crystallinity, grain size and surface morphology of Zn$_{(1-x)}$Zr$_x$O films were discussed. Zn$_{(1-x)}$Zr$_x$O-TFTs exhibited much lower off-state current (I_{OFF}) and higher on/off ratio than pure ZnO-TFT. The behavior of I_{OFF} related to the carrier concentration (n) of Zn$_{(1-x)}$Zr$_x$O films and the correlation between n and grain size were interpreted. The optimized I_{OFF} and on/off ratio of Zn$_{(1-x)}$Zr$_x$O-TFT were 3.24×10^{-13} A/μm and 8.89×10^{6} where $x = 0.03$, respectively.

4.1 Introduction

ZnO is an *n*-type, wide band gap semiconductor with various applications, such as varistors, acoustic wave devices [1] and light emitting diodes [2]. Recently, ZnO utilized as active channel layers (ACLs) in thin-film transistors (TFTs) have attracted much attention due to its

transparency and low processing temperature. Most of the ZnO-based TFTs were realized by laser molecular-beam epitaxy [3], sputtering [4-9] or pulsed-laser deposition (PLD) [10,11], and the mobility ranging from 0.05 to 70 cm^2/Vs were obtained among the studies. Besides the fabrication of ZnO ACLs in TFTs involving vacuum facilities mentioned above, some studies demonstrated another deposition method, chemical solution deposition (CSD), to fabricate ZnO ACL in TFTs. Ohya [12] and Norris [13] *et al.* reported that ZnO-TFTs had been prepared by CSD process through dip and spin-coating methods, respectively. For large area flat-panel display fabrication, the CSD process provides a more efficient way to deposit device components than vacuum techniques. Nevertheless, ZnO-based TFTs reveal large off-state current since the channel is conductive without applying gate bias. This phenomenon may attribute to the as-deposited ZnO thin films containing high carrier densities, thus increase the conductivity in the channel. Hence, one of the most important works in ZnO-based TFTs researches is to reduce the carrier concentration in ZnO thin films. Since it has been demonstrated that the ZnO films exhibited lower carrier concentration with higher annealing temperature [14], Norris *et al.* employed CSD process to prepare ZnO-TFTs by using rapid thermal anneal at a temperature of 700℃ and obtain a very low off-state current about 1pA. It also has been demonstrated that the electrical characteristics of ZnO thin films could be widely controlled via doping impurity atoms. For instance, ZnO thin films become highly conductive electrodes by doping Al [15] or Ga [16] and become *p*-type semiconductors by co-doping P and Mg atoms [17]. In this study, we investigated the properties of sol-gel derived

Zr-doped ZnO films at a low annealing temperature of 500℃, and the

effects on the electrical performance of Zn$_{(1-x)}$Zr$_x$O-TFTs were also

discussed.

4.2 Experiment

The Zn$_{(1-x)}$Zr$_x$O sol-gel precursors were synthesized by mixing of zinc

acetate {Zn(CH$_3$COO)$_2$ · 2H$_2$O} and zirconium isopropoxide

{Zr[(CH$_3$)$_2$CHO]$_2$} dissolved in 2-methoxyethanol and monoethanolamine

(MEA), and the solutions were stirring at 60℃ for 30 minutes. The

nominally *x* value for Zn$_{(1-x)}$Zr$_x$O was ranged from 0 to 0.10, and the total

metal ions concentration was maintained at 0.75 mol/l. Zn$_{(1-x)}$Zr$_x$O thin

films were deposited using the sol-gel solution by spin coating method.

After coating, the films were immediately dried at 400℃ for 30 minutes,

and then annealed in a tube furnace at 500℃ for 4 hours under oxygen

ambient. The molar fractions of Zr in Zn$_{(1-x)}$Zr$_x$O films were determined by

inductively coupled plasma-atomic emission spectrometer (ICP-AES) by

dissolving the films in HNO$_3$ solution. The crystallinity of Zn$_{(1-x)}$Zr$_x$O thin

films was examined by X-ray diffraction (XRD, Siemens D5000) with Cu

Kα radiation. The microstructure and surface morphology were observed

by scanning electron microscope (SEM, Hitachi S-4700) and atomic-force

microscope (AFM, Digital Instruments Nanoscope III). The dielectric

constants of Zn$_{(1-x)}$Zr$_x$O films were performed by capacitance-voltage (*C-V*)

characteristics with a Keithley 590 *C-V* Analyzer, a 595 *C-V* Quasi Meter and a 230 Voltage Source from the MIM capacitance structure ($Pt/Zn_{(1-x)}Zr_xO/Pt$). The charge carrier concentration *n* of $Zn_{(1-x)}Zr_xO$ films were measured by the same *C-V* measurement system with a metal-oxide-semiconductor (MOS) structure of $Al/SiO_2/Zn_{(1-x)}Zr_xO/Pt$. The MIM and MOS structure were both deposited on oxidized silicon substrates. The device structure of $Zn_{(1-x)}Zr_xO$-TFTs as shown in Figure 4-1 is bottom-gate type and was fabricated by the following sequence of process. The metal chromium was deposited by sputtering on the glass substrate as a bottom gate electrode. Silicon dioxide served as the gate insulator with a thickness of 3000 Å by using plasma-enhanced chemical vapor deposition (PECVD). The source and drain electrodes were made up of indium-tin oxide (ITO) and channel width and length were 500 μm and 50 μm, respectively. Finally, the $Zn_{(1-x)}Zr_xO$ thin films were deposited by spin coating with the same processing parameters mentioned above.

4.3 Results and discussion

Figure 4-2 shows the XRD patterns of the $Zn_{(1-x)}Zr_xO$ thin films after annealing at 500℃ with various mole fraction *x* ranging from 0 to 0.10. It can be seen that all of the compositions exhibited (100), (002) and (101) peaks belonged to the hexagonal wurtzite structure of ZnO, and no ZrO_2 peaks were detected in the XRD spectra. For *x* = 0.01, the orientation of (002) was slightly increased but (100) and (101) were decreased compared with the pure ZnO film. All of the intensity of orientations decreased while

the x value was more than 0.03. It is considered that the decrease of orientation intensity of Zn$_{(1-x)}$Zr$_x$O films may result from the impurities of Zr dopant thus degraded the crystal structure.

Figure 4-3 (a)-(d) shows the surface images of pure ZnO and $x = 0.03$ in Zn$_{(1-x)}$Zr$_x$O films observed by using SEM and AFM, which depicted the influence of the Zr additives on the surface morphologies of Zn$_{(1-x)}$Zr$_x$O thin films. Chain-like structure and a small grain size of 50 nm can be observed in pure ZnO, as shown in Figure 4-3 (a). In contrast, the average grain size was reduced to about 10 nm for $x = 0.03$ in Zn$_{(1-x)}$Zr$_x$O films. Since the grain size was reduced by doping Zr in Zn$_{(1-x)}$Zr$_x$O films, the Zn$_{(1-x)}$Zr$_x$O films had poorer crystallinity with higher x value. This result was in good agreement with the XRD data. In addition, the surface roughness of the pure ZnO ($R_{rms} = 44$ nm) was much greater than $x = 0.03$ of Zn$_{(1-x)}$Zr$_x$O films ($R_{rms} = 6$ nm) observed by AFM [Figure 4-3 (c) and (d)]. The reduction of surface roughness may also result from the decrease of grain size for Zr doping.

The sol-gel-derived Zn$_{(1-x)}$Zr$_x$O thin films were also characterized by XPS to study the binding energy and chemical shift of the elements in the Zn$_{(1-x)}$Zr$_x$O films. Figure 4-6 and 4-7 shows the XPS survey scan analysis of the un-doped ZnO and Zn$_{(1-x)}$Zr$_x$O films, where x ranged from 0.10 to 0.10, respectively. Figure 4-6 displays that there are Zn, O, and C elements in the un-doped ZnO films. The detection of small amounts of carbon could be attributed to the residual precursor and reactant adsorbed on the surface. The two strong peaks located around 531 and 1022 eV, respectively, as shown in Figure 4-6 and 4-7 agree with the O 1s and Zn 2p$_{3/2}$ binding

energy for ZnO. Figure 4-7b, c, and d show the appearance of the Zr 3d peak when $x \geq$ 0.03. Figure 4-8 shows XPS spectra of O 1s of Zn$_{(1-x)}$Zr$_x$O thin films, where x ranged from 0.00 to 0.10. The typical O 1s peak in the surface could be fitted by two nearly Gaussian, centered at 531 and 532.8 eV, in all spectra. The component on the low binding energy side of the O 1s spectrum at 531 eV is attributed to O^{2-} ions on wurtzite structure of hexagonal Zn^{2+} ion array, surrounded by Zn atoms with their full complement of nearest-neighbor O^{2-} ions [18-20]. In other words, the intensity of this component is the measure of the amount of oxygen atoms in a fully oxidized stoichiometric surrounding. The higher binding energy component located at 532.8 eV is usually attributed to the presence of loosely bound oxygen on the surface of the Zn$_{(1-x)}$Zr$_x$O films, belonging to a specific species, e.g., -CO$_3$, adsorbed H$_2$O or adsorbed O$_2$ [21,22]. Figure 4-8 shows that the O 1s peak position have no significantly shift when the Zr content was increased, unlike the case of Zn$_{(1-x)}$Mg$_x$O. This phenomenon indicates that the number of oxygen atoms in higher Zr content of Zn$_{(1-x)}$Zr$_x$O films have no obviously increase. Figure 4-9 shows the relative intensity of the O 1s peak as a function of the x values in Zn$_{(1-x)}$Zr$_x$O films, and it could be observed that the relative intensity of the O 1s peak did not increase with higher x values. This result reveals that the amount of O^{2-} ions that bonding with wurtzite structure of hexagonal Zn^{2+} ions were not increased. Figure 4-10 displays the XPS spectra of Zn 2p$_{3/2}$ of Zn$_{(1-x)}$Zr$_x$O thin films, where x ranged from 0.00 to 0.10. The peak position corresponding to Zn 2p$_{3/2}$ has no significantly variation, which is indicative of no more zinc atoms being bound to oxygen atoms [23]. From the XPS

data, it is considered that there are no more oxygen atoms exist in higher Zr content thin films. Furthermore, the amounts of bonding between oxygen and zinc also have no obviously increase with higher Zr content. Therefore, the number of defects, including oxygen vacancies and interstitial zinc atoms, were not diminished by means of doping Zr. Figure 4-11 shows the XPS spectra of Zr 3d of Zn$_{(1-x)}$Zr$_x$O thin films, which x ranged from 0.10 to 0.10. The peaks at 185.8 and 183.5 eV corresponding to Zr 3d$_{3/2}$ and Zr 3d$_{5/2}$, respectively, have no significantly shift.

Figure 4-12 shows the drain current-drain voltage (I_D-V_D) characteristics of (a) pure ZnO and (b) x = 0.03 of Zn$_{(1-x)}$Zr$_x$O-TFTs. The output characteristics of pure ZnO-TFT revealed large drain current at a gate voltage of V_G = 0V. This indicated that pure ZnO-TFT exhibited a normally on device feature. Moreover, pure ZnO-TFT presented poorer saturation current than Zn$_{(1-x)}$Zr$_x$O-TFT where x = 0.03. Figure 4-13 shows the drain current-gate voltage (I_D-V_G) characteristics of Zn$_{(1-x)}$Zr$_x$O-TFTs with V_{DS} = 100 V, where x was varied from 0 to 0.10. It can be seen that the minimum drain current (I_{OFF}) measured at a drain voltage of V_{DS} = 100 V decreased dramatically with more Zr doping. Even though the maximum drain current (I_{ON}) slightly decreased with higher Zr content, the I_{ON}/I_{OFF} current ratio had a significant increase via Zr doping. The maximum I_{ON}/I_{OFF} of Zn$_{(1-x)}$Zr$_x$O-TFTs where x = 0.03 was 8.89 $\times$ 10^6 which more than five orders of magnitude larger than pure ZnO-TFT. The device characteristics of Zn$_{(1-x)}$Zr$_x$O-TFTs were summarized in Table 4-1 extracted form the results shown in Figure 4-13. The saturation mobility (μ_{sat}) and threshold voltage (V_{th}) was calculated from the slopes and intercepts of

$\sqrt{I_D} - V_G$ plots at $V_{DS} = 100$ V, respectively. As shown in Table 4-1, the μ_{sat} decreased with higher x value due to the Zr impurities acted as scattering centers for carrier transportation. Another reasonable explanation for Zr doped ZnO films had lower μ_{sat} than pure ZnO films is that the former had poorer crystallinity and smaller grain size than the later form the data of XRD and surface images.

The carrier concentration n of semiconductors can be estimated by the measurement of capacitance-voltage characteristics of Schottky or MOS structure. For a MOS structure, the carrier concentration is given by $n = -2\left[q\varepsilon_s\left(dC^{-2}/dV\right)\right]^{-1}$, where q is the electron charge and ε_s is the permittivity of the semiconductor. The values of dielectric constant of the Zn$_{(1-x)}$Zr$_x$O thin films obtained from the capacitance of MIM (Pt/Zn$_{(1-x)}$Zr$_x$O/Pt) structure were 8.90, 9.17, 9.33, 9.56 and 9.79 for $x =$ 0.00, 0.01, 0.03, 0.05 and 0.10, respectively. Figure 4-15 shows the carrier concentration n of Zn$_{(1-x)}$Zr$_x$O thin films as a function of the value x. It can be seen that the carrier concentration decreased with more Zr additive. Previous study has indicated that higher carrier concentration in ACL might result in larger off-state current and normally on device characteristic [24]. Hence, the I_{OFF} of Zn$_{(1-x)}$Zr$_x$O-TFTs was significantly suppressed owing to the reduction of carrier concentration of Zn$_{(1-x)}$Zr$_x$O thin films with more Zr content. Furthermore, the decrease of carrier concentration in Zn$_{(1-x)}$Zr$_x$O thin films might attribute to the reduction of grain size. A modeling of polycrystalline ZnO-TFTs provided by Hossain [25] indicated that smaller grain size of ACLs led to larger activation energy (E_a) between conduction

band (E_c) and Fermi level (E_f), i.e., $E_a = E_c - E_f$, thus the concentration of

thermally activated carrier became smaller according to the equation of

$n = N_C \exp\left[-\left(E_c - E_f\right)/kT\right]$, where N_C is the effective density of states for

electrons. Therefore, it was observed that the carrier concentration of the

ZnO films was suppressed and well controlled around 10^{16} cm^{-3} by doping

Zr ions at a low temperature of 500℃. Moreover, the reduction of carrier

concentration in Zn$_{(1-x)}$Zr$_x$O films as shown in Figure 4-15 also affected the

behaviors of V_{th} of the device as listed in Table 4-1. The device feature of

un-doped ZnO TFT revealed depletion-mode characteristics as shown in

Figure 4-12 (a), and this phenomenon could attribute to the high carrier

concentration in the un-doped ZnO films. Thus the resistivity of un-doped

ZnO active channel layer is low and large drain current flows at V_G = 0V.

Hence, a negative gate bias was required to deplete the free carriers in the

channel to turn off the device and brought about a negative V_{th} of un-doped

ZnO-TFT. On the other hand, the carrier concentration of Zr doped ZnO

films were diminished due to the reduction of the grain size. The lower

carrier concentration of Zn$_{(1-x)}$Zr$_x$O films gave rise to the higher resistivity

of Zn$_{(1-x)}$Zr$_x$O active channel layers and finally made the Zn$_{(1-x)}$Zr$_x$O films

become semi-insulating with high x values. Thus, a positive gate voltage

was required to induce enough free carriers in the channel to turn on the

device and led to a positive V_{th}. Therefore, the V_{th} corresponded to lower x

values were negative and increased to positive with higher x values as

shown in Table 4-1. The ZnO-TFT models reported by Hossain were also

consistent with this explanation. Modeled transfer characteristics of

ZnO-TFT depicted that the V_{th} shifts to the positive direction of gate voltage while the grain size of ZnO films decreased. Figure 4-14 shows the capacitance-voltage characteristics and a plot of $1/C^2$ as a function of voltage of Zn$_{(1-x)}$Zr$_x$O MOS structure where $x = 0.03$. A uniform carrier distribution can be observed of Zn$_{(1-x)}$Zr$_x$O semiconductor form Figure 4-14.

4.4 Conclusion

In conclusion, we found that the crystallinity of sol-gel derived Zn$_{(1-x)}$Zr$_x$O thin films degraded with more Zr dopant, and the grain size and surface roughness also decreased with higher x values of Zn$_{(1-x)}$Zr$_x$O thin films. The off-state current of Zn$_{(1-x)}$Zr$_x$O-TFTs was dramatically suppressed due to the reduction of carrier concentration in Zn$_{(1-x)}$Zr$_x$O active channel layers with more Zr additive. It was also demonstrated that the carrier concentration of sol-gel derived ZnO films could be diminished by doping Zr ions instead of high temperature annealing. The reduction of carrier concentration might result from the decrease of grain size. The optimized I_{OFF} and on/off current ratio of Zn$_{(1-x)}$Zr$_x$O thin films where $x = 0.03$ were 3.24×10^{-13} A/μm and 8.89×10^6, respectively.

References

[1] N. W. Emanetoglu, J. Zhu, Y. Chen, J. Zhong, Y. Chen, and Y. Lu, *Appl. Phys. Lett.* **85**, 3702 (2004).

[2] R. F. Service, *Science* **276**, 895 (1997).

[3] T. I. Suzuki, A. Ohtomo, A. Tsukazaki, F. Sato, J. Nishii, H. Ohno and M. Kawasaki, *Adv. Mater.* **16**, 1887 (2004).

[4] P. F. Carcia, R. S. McLean, M. H. Reilly, and G. Nunes, Jr, *Appl. Phys. Lett.* **82**, 1117 (2003).

[5] H. S. Bae, M. H. Yoon, J. H. Kim, and Seongil Im, *Appl. Phys. Lett.* **83**, 5313 (2003).

[6] R. L. Hoffman, *J. Appl. Phys.* **95**, 5813 (2004).

[7] E. M. C. Fortunato, P. M. C. Barquinha, A. C. M. B. G. Pimentel, A. M. F. Gonçalves, A. J. S. Marques, R. F. P. Martins, and L. M.N. Pereira, *Appl. Phys. Lett.* **85**, 2541 (2004).

[8] H.S. Bae, Seongil Im, *Thin Solid Films*, **469-470**, 75 (2004).

[9] H. S. Bae, J. H. Kim, and Seongil Im, Electrochem. *Solid State Lett.* **7**, G279 (2004).

[10] J. Nishii, F. M. Hossain, S. Takagi, T. Aita, K. Saikusa, Y. Ohmaki, I. Ohkubo, S. Kishimoto, A. Ohtomo, T. Fukumura, F. Matsukura, Y. Ohno, H. Koinuma, H. Ohno and M. Kawasaki, *Jpn. J. Appl. Phys.* **42**, L347 (2003).

[11] S. Masuda, K. Kitamura, Y. Okumura, S. Miyatake, H. Tabata and T. Kawai, *J. Appl. Phys.* **93**, 1624 (2003).

[12] Y. Ohya, T. Niwa, T. Ban and Y. Takahashi, *Jpn. J. Appl. Phys.* **40**, 297 (2001).

[13] B. J. Norris, J. Anderson, J. F. Wager and D. A. Keszler, *J. Phys. D: Appl. Phys.* **36**, L105 (2003).

[14] H. S. Kang, J. S. Kang, J. W. Kim, and S. Y. Lee, *J. Appl. Phys.* **95**, 1246 (2004).

[15] C. Agashe, O. Kluth, J. Hu¨pkes, U. Zastrow, B. Rech and M. Wuttig, *J. Appl. Phys.* **95**, 1911 (2004).

[16] X. Yu, J. Ma, F. Ji, Y. Wang, X. Zhang, C. Cheng and H. Ma, *Appl. Surf. Sci.* **239**, 222 (2005).

[17] Y. W. Heo, Y. W. Kwon, Y. Li, S. J. Pearton, and D. P. Norton, *Appl. Phys. Lett.* **84**, 3474 (2004).

[18] R. Cebulla, R. Weridt, and K. Ellmer, *J. Appl. Phys.*, **83** 1087 (1998).

[19] T. Szorenyi, L. D. Laude, I. Bertoti, Z. Kantor, and Z. Geretovszky, *J. Appl. Phys.*, **78** 6211 (1995).

[20] L. K. Rao, and V. Vinni, *Appl. Phys. Lett.*, **63** 608 (1993).

[21] S. Major, S. Kumar, M. Bhatnagar, and K. L. Chopra, *Appl. Phys. Lett.*, **40** 394 (1986).

[22] M. N. Islam, T. B. Ghosh, K. L. Chopra, and H. N. Acharya, *Thin Solid Films*, **280** 20 (1996).

[23] W. G. Han, S. G. Kang, T. W. Kim, D. W. Kim, and W. J. Cho, *Appl. Surf. Sci.*, **245** 384 (2005).

[24] K. Nomura, H. Ohta, A. Takagi, T. Kamiya, M. Hirano and H. Hosono, *Nature* **432**, 488 (2004).

[25] F. M. Hossain, J. Nishii, S. Takagi, A. Ohtomo, T. Fukumura, H. Fujioka, H. Ohno, H. Koinuma and M. Kawasaki, *J. Appl. Phys.* **94**, 7768 (2003).
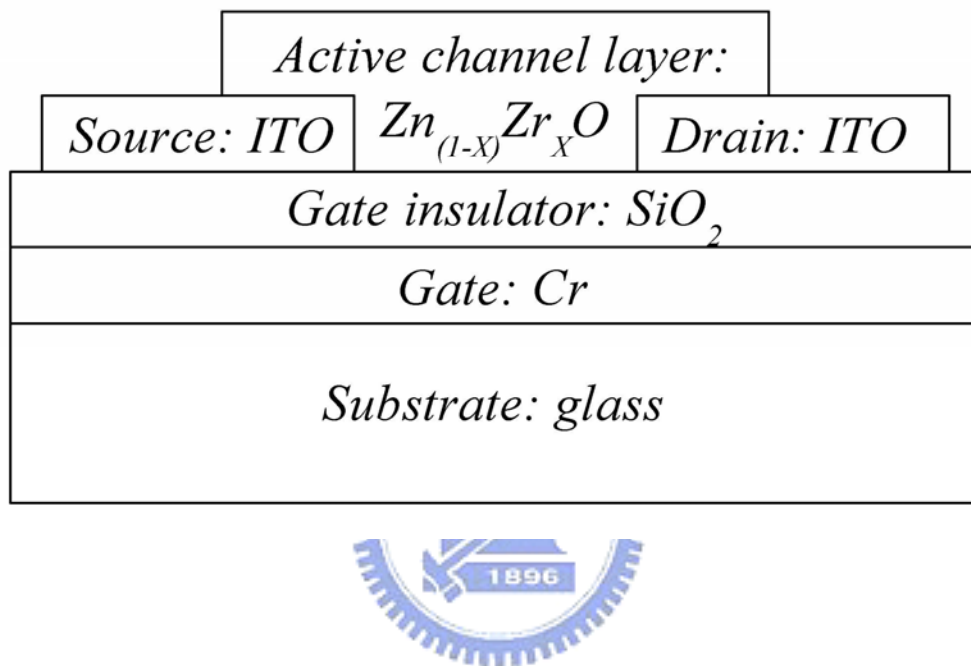
Figure 4-1 Schematic diagram of TFT utilized Zn$_{(1-x)}$Zr$_x$O films as active
channel layer.
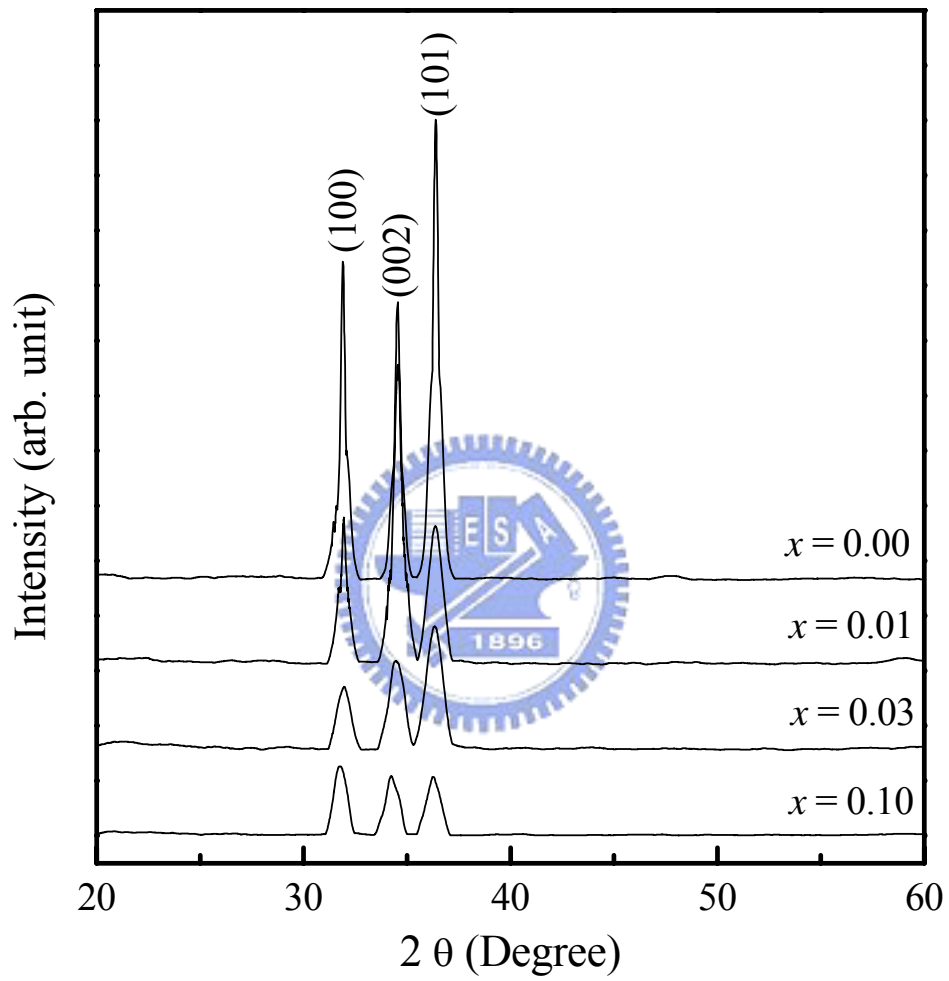
Figure 4-2 XRD spectra of Zn$_{(1-x)}$Zr$_x$O thin films annealed at 500℃ for 4h.
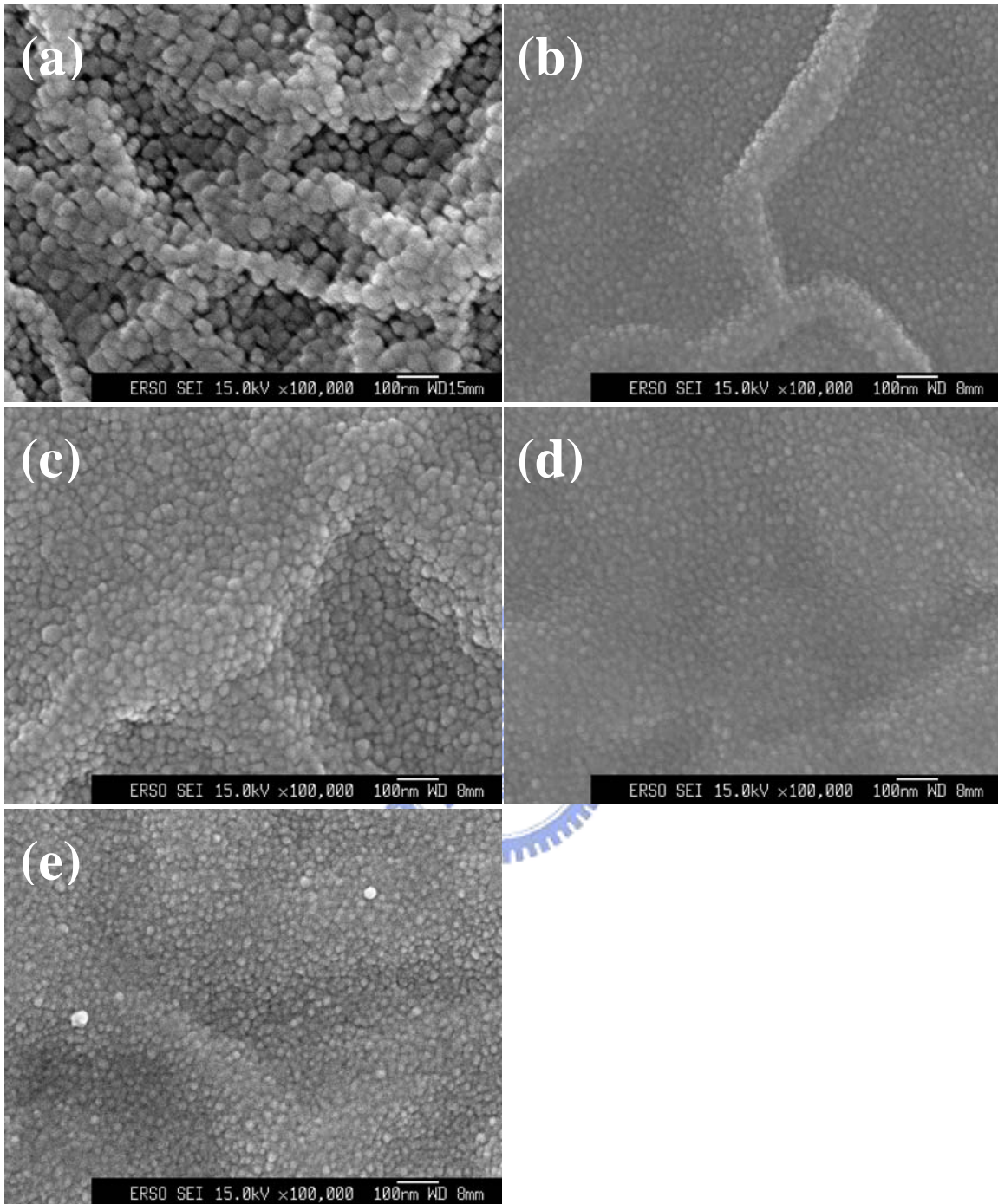
Figure 4-3 SEM surface images of Zn$_{(1-x)}$Zr$_x$O thin films of (a) x = 0.00, (b) x = 0.01, (c) x = 0.03, (d) x = 0.05, and (e) x = 0.10.
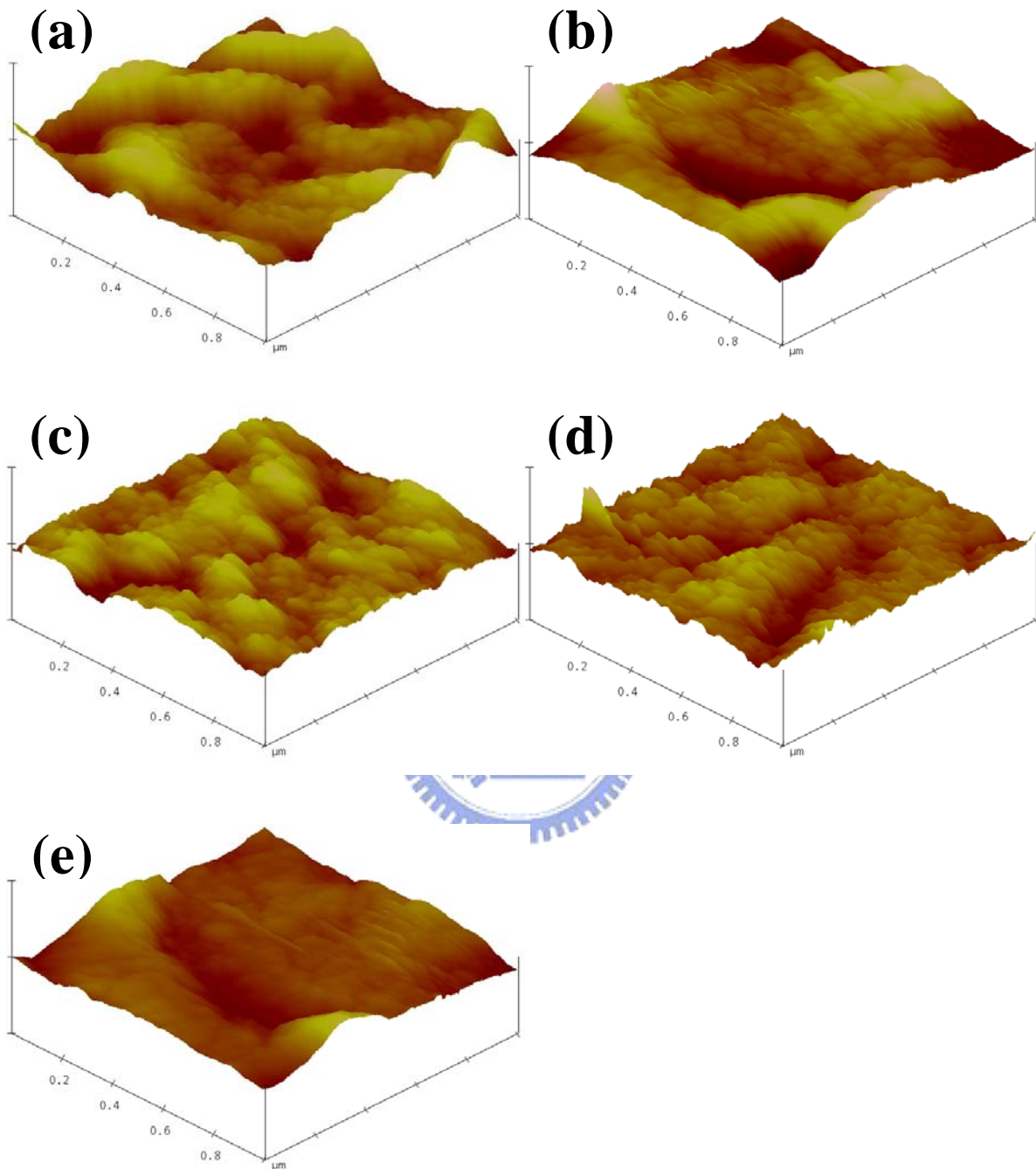
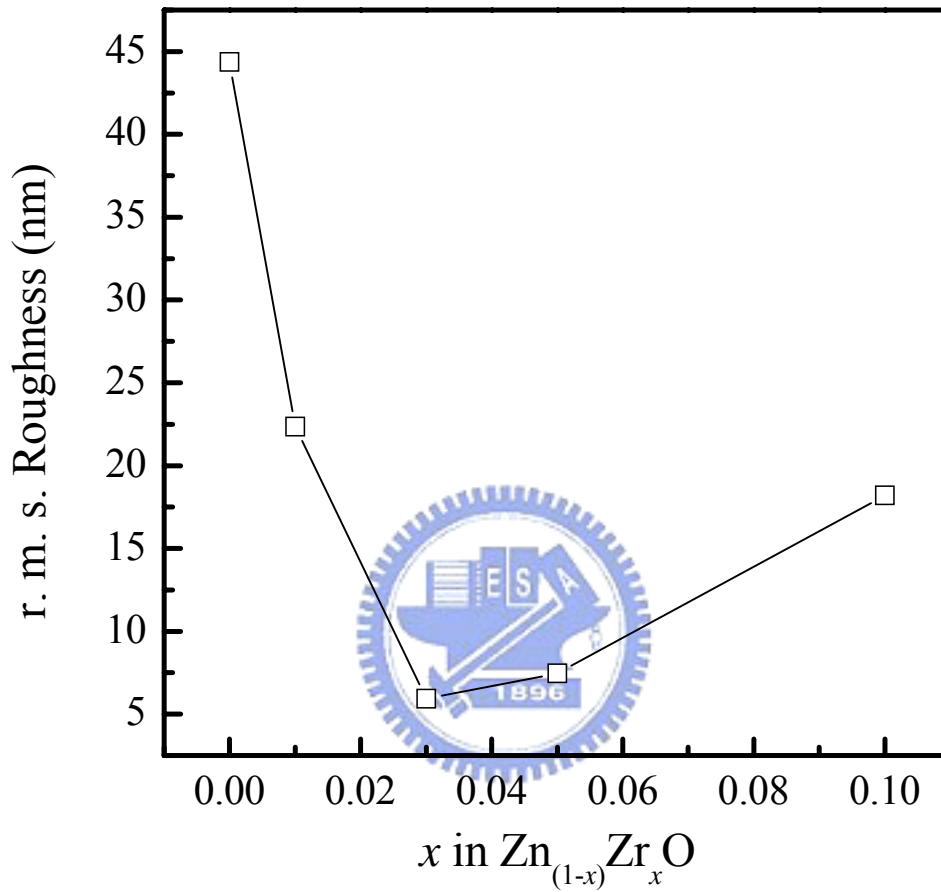Figure 4-4 AFM surface morphologies of Zn$_{(1-x)}$Zr$_x$O thin films of (a) x = 0.00, (b) x = 0.01, (c) x = 0.03, (d) x = 0.05, and (e) x = 0.10.

Figure 4-5 Roughness of Zn$_{(1-x)}$Zr$_x$O films as a function of the Zr content.
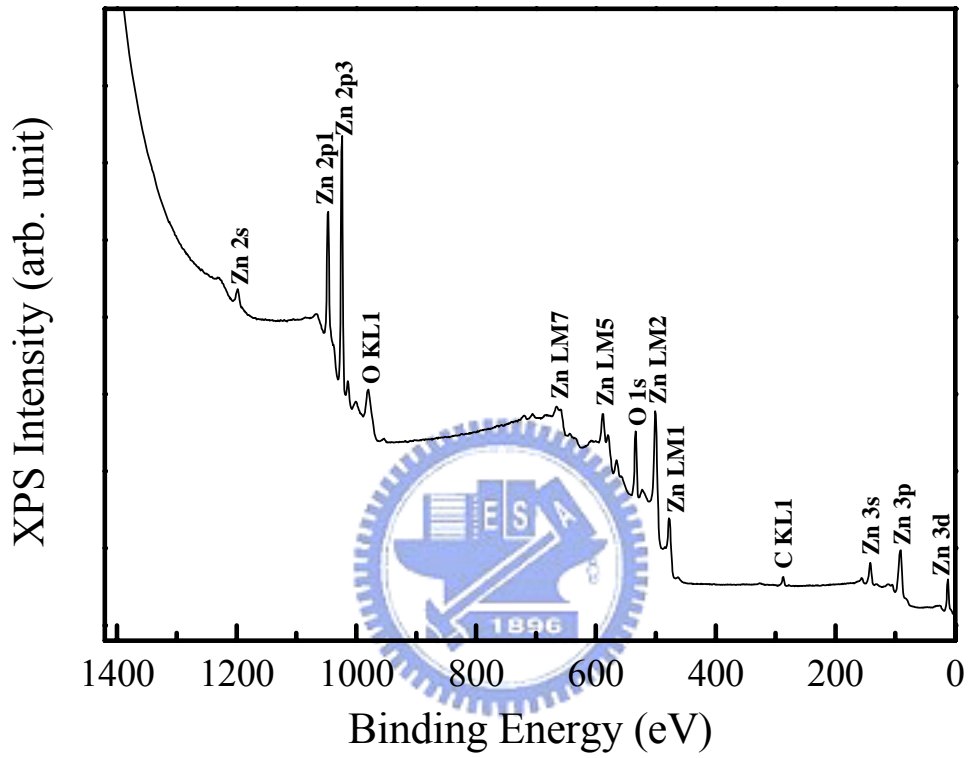
Figure 4-6 XPS survey scan analysis of un-doped ZnO thin film annealed

at 500℃ under oxygen atmosphere for 2 hr.

(a)   **(b)**

(c)   **(d)**
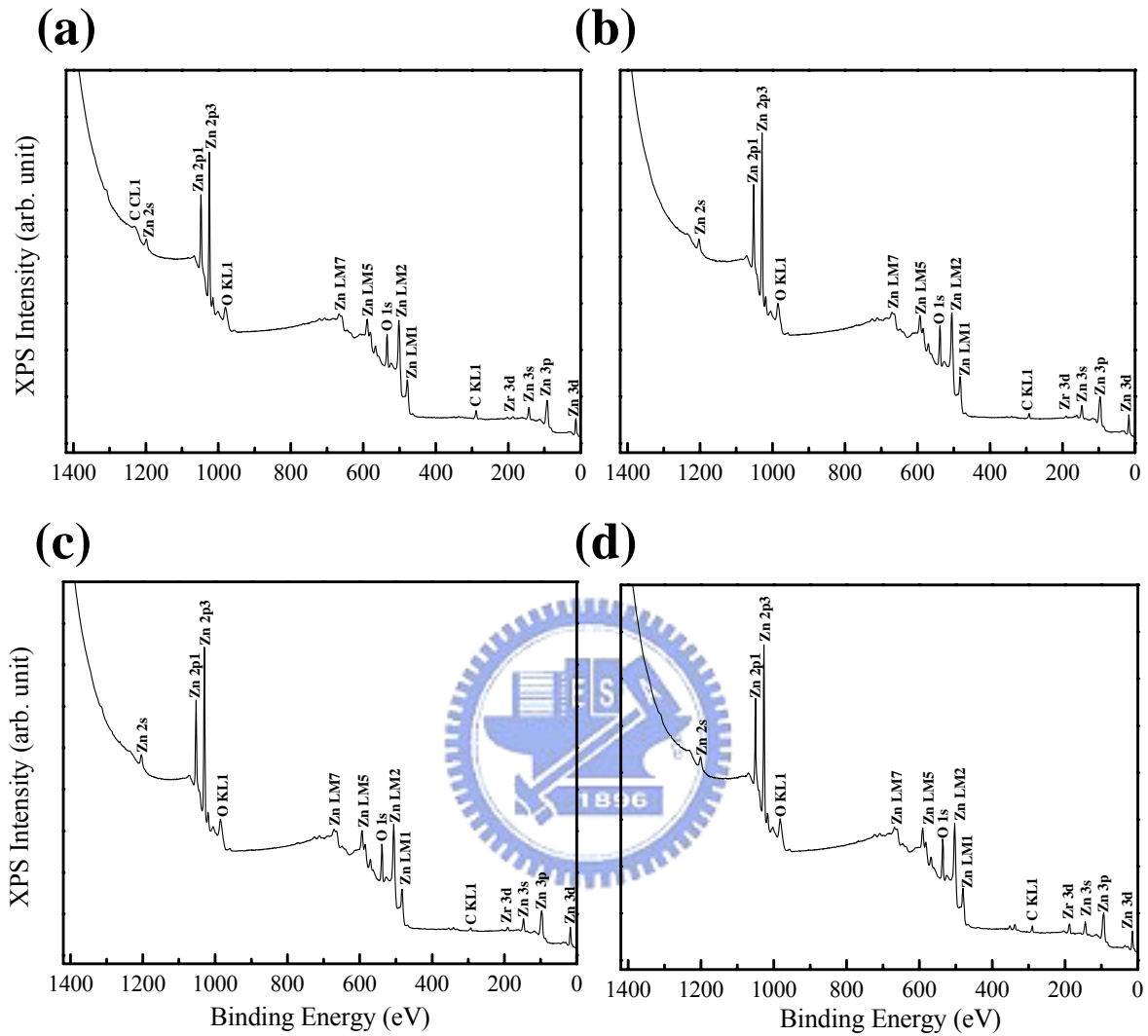
Figure 4-7 X-ray photoelectron spectroscopy survey scan analysis of Zn$_{(1-x)}$Zr$_x$O thin films of (a) $x = 0.01$, (b) $x = 0.03$, (c) $x = 0.05$, and (d) $x = 0.10$.
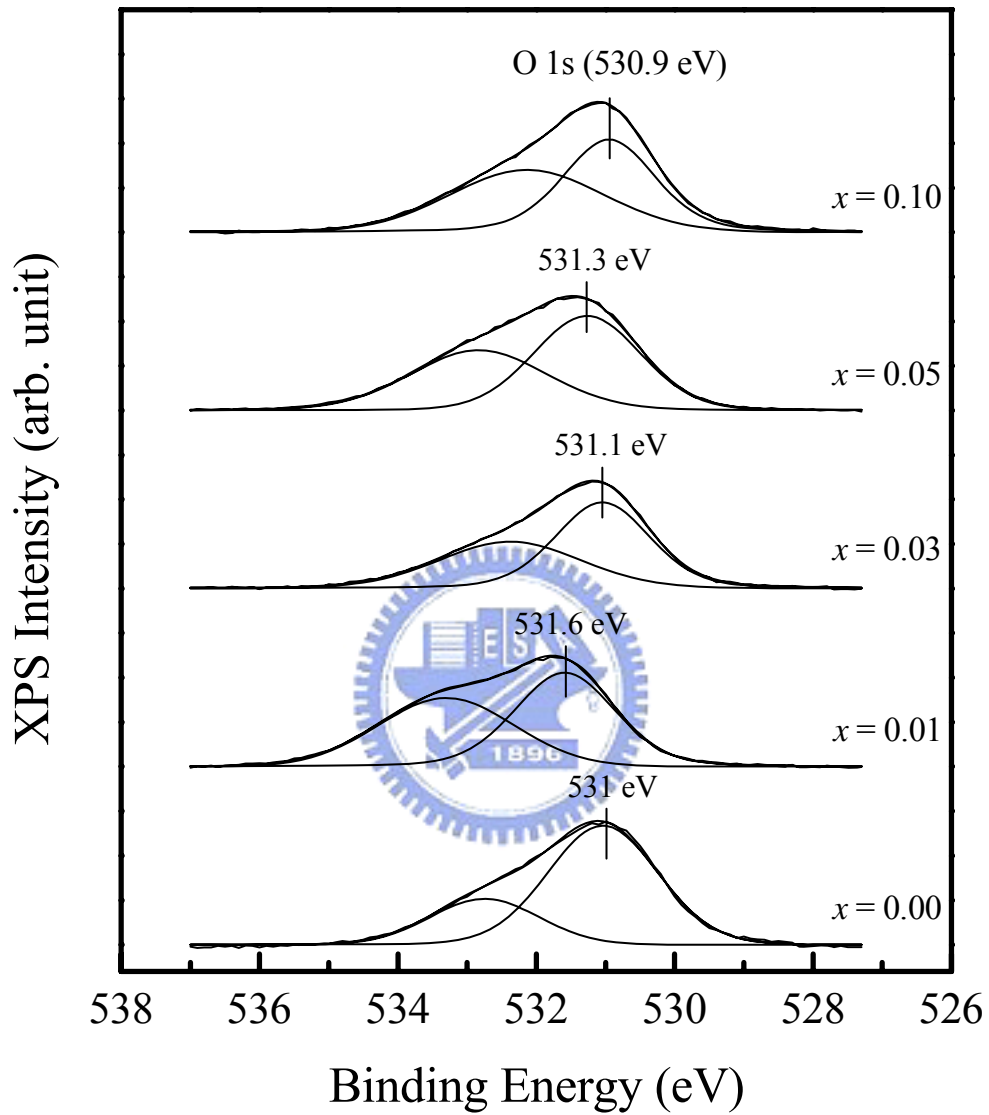
Figure 4-8 X-ray photoelectron spectroscopy spectra of O 1s of $Zn_{(1-x)}Zr_xO$
thin films, where *x* ranged from 0.00 to 0.10.
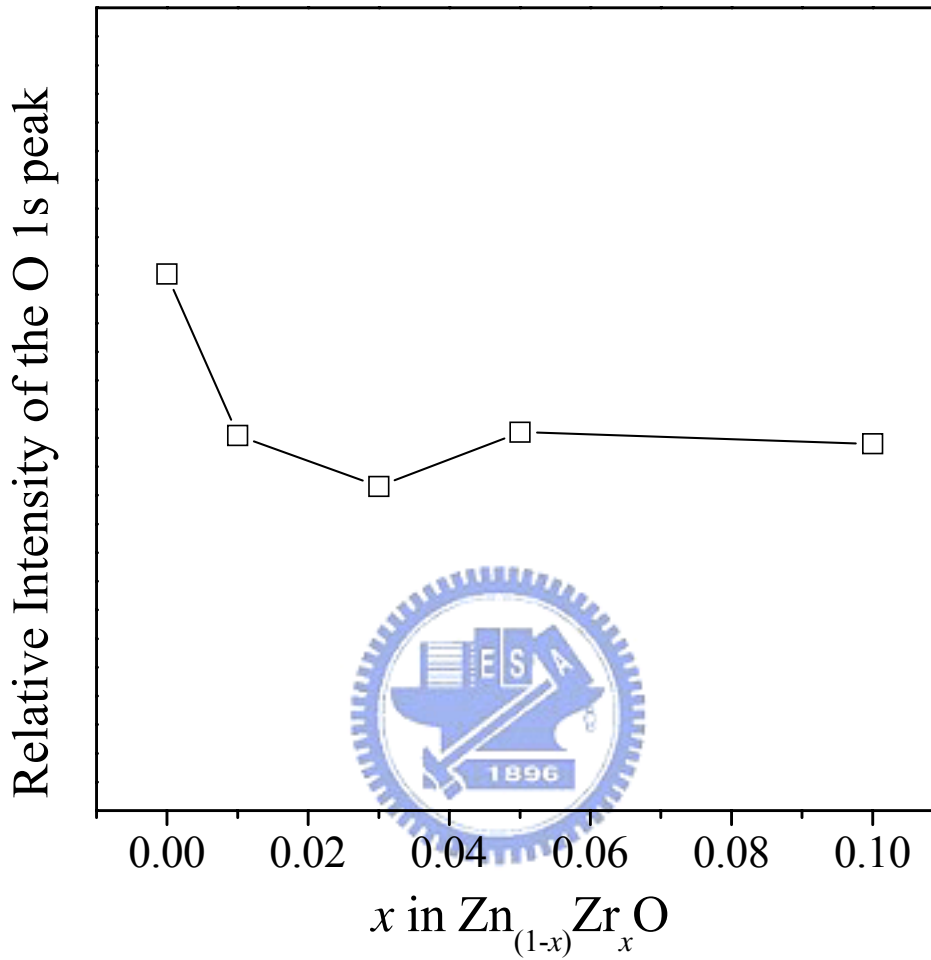
Figure 4-9 Dependence of relative intensity of the O 1s peak of the Zn$_{(1-x)}$Zr$_x$O thin films, on the values of *x*.
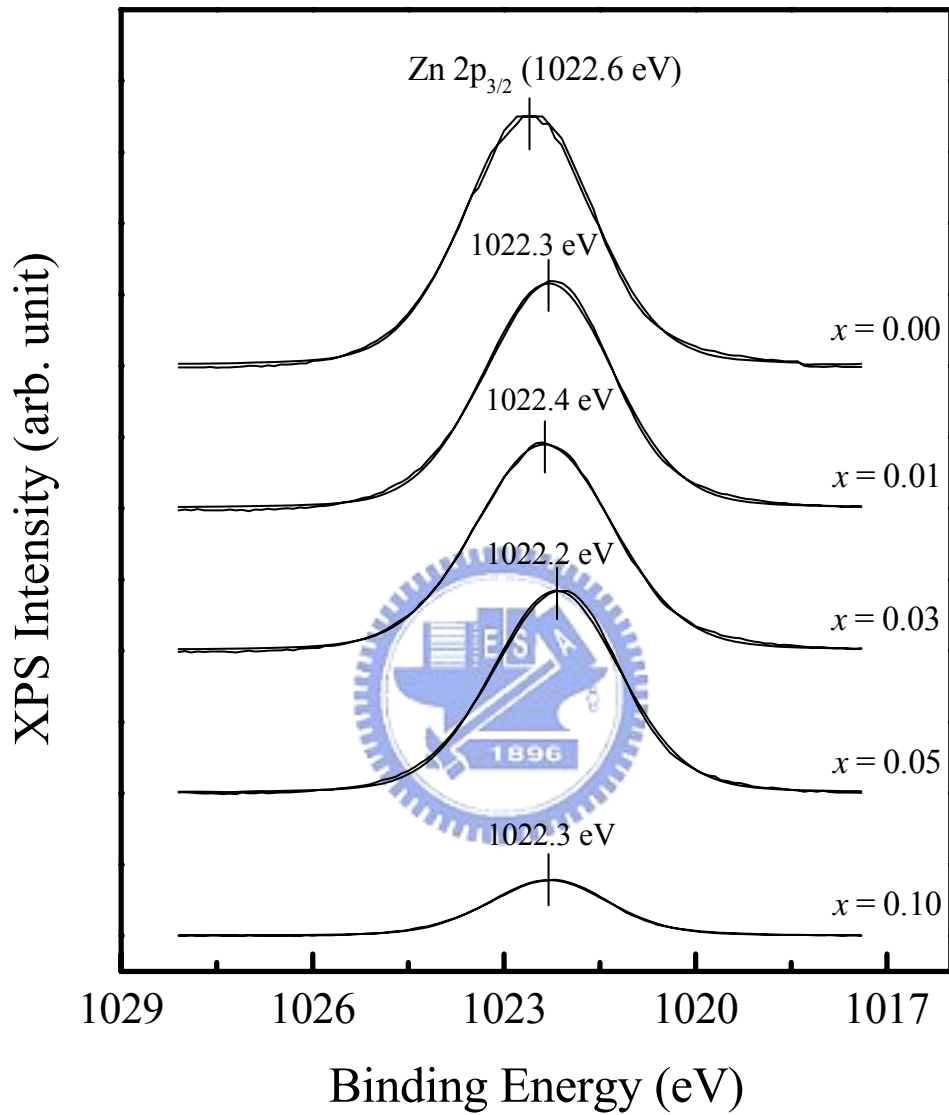
Figure 4-10 X-ray photoelectron spectroscopy spectra of Zn 2p$_{3/2}$ of Zn$_{(1-x)}$Zr$_x$O thin films, where *x* ranged from 0.00 to 0.10.
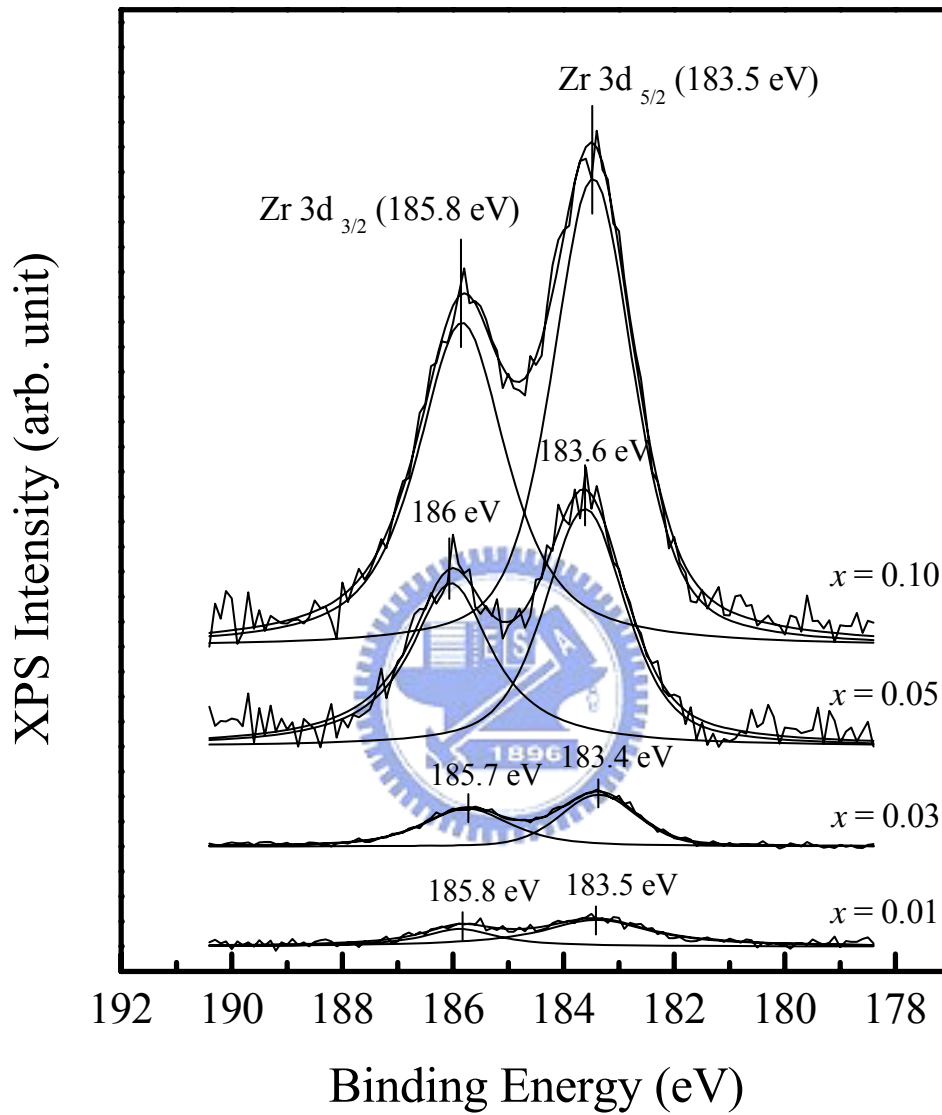
Figure 4-11 X-ray photoelectron spectroscopy spectra of Zr 3d$_{3/2}$ and Zr 3d$_{5/2}$ of Zn$_{(1-x)}$Zr$_x$O thin films, where *x* ranged from 0.10 to 0.10.
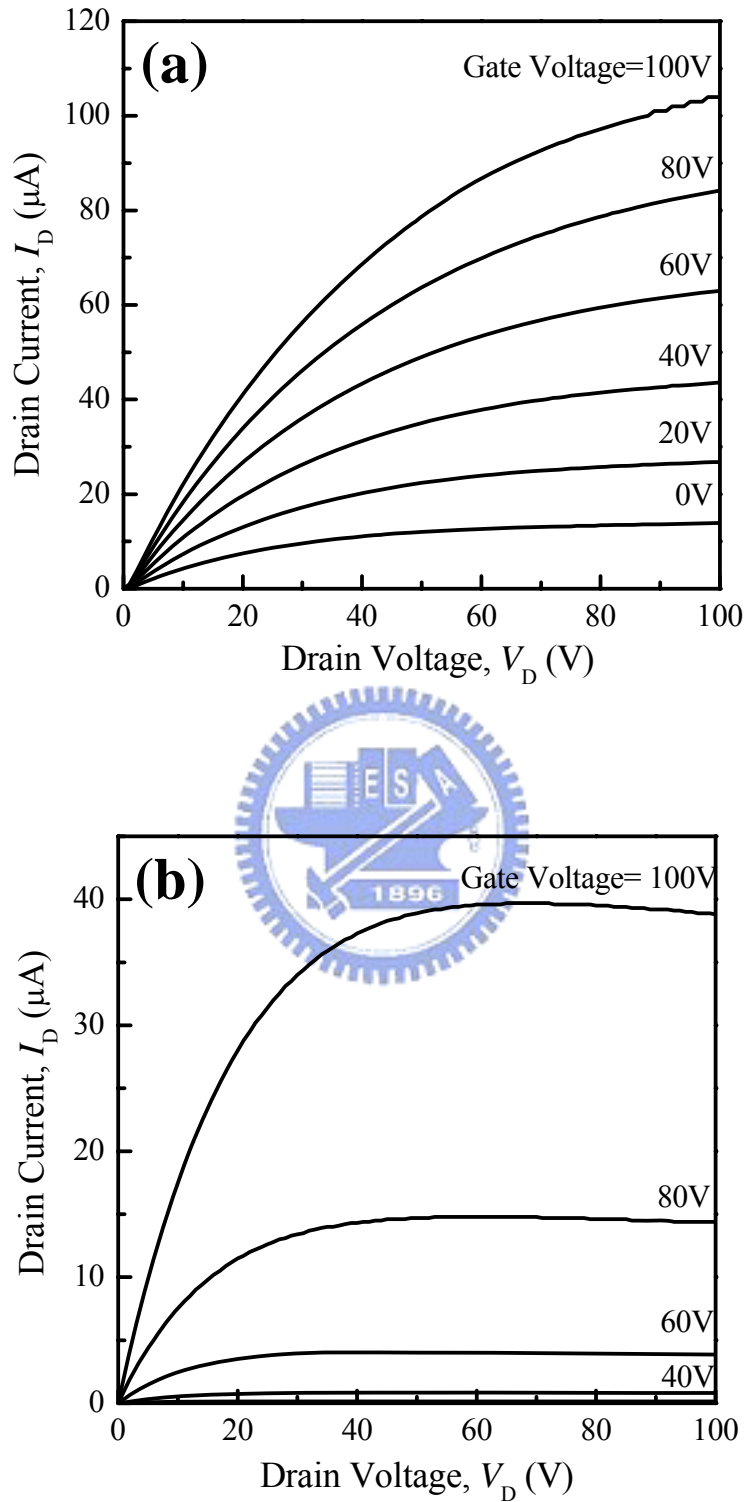
Figure 4-12 Output characteristics of Zn$_{(1-x)}$Zr$_x$O-TFTs of (a) x = 0.00 and
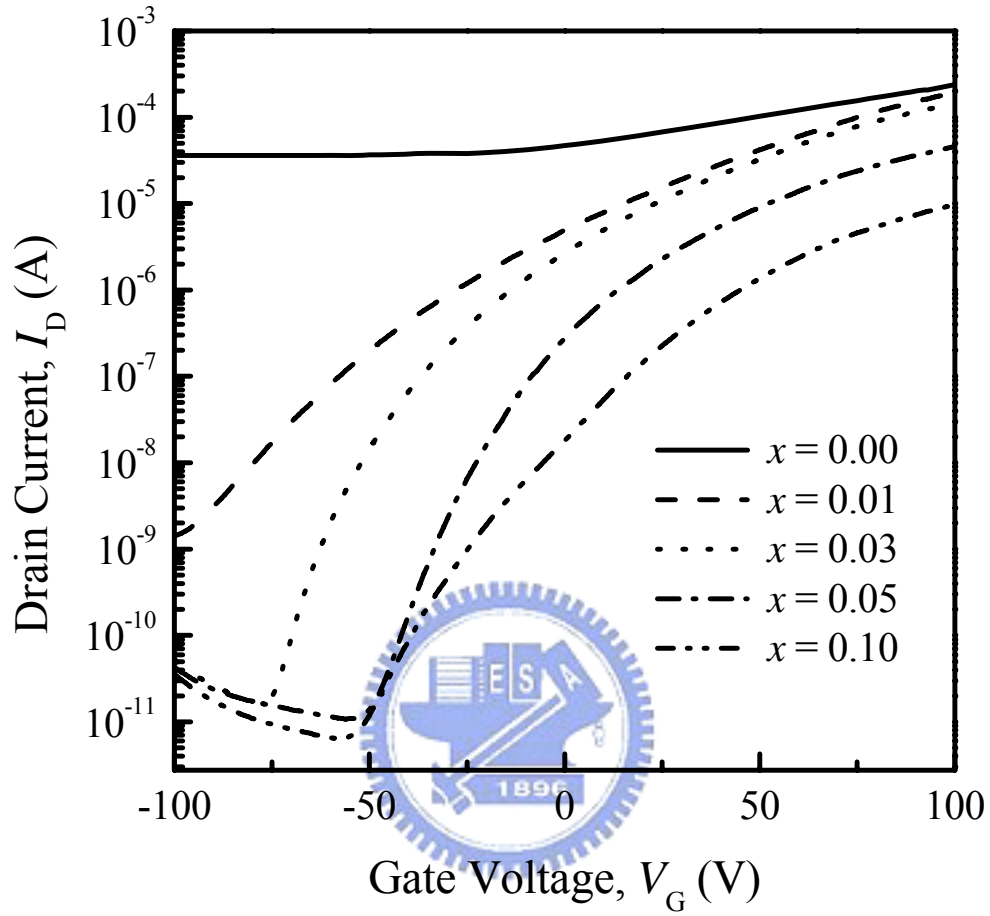
(b) x = 0.03.

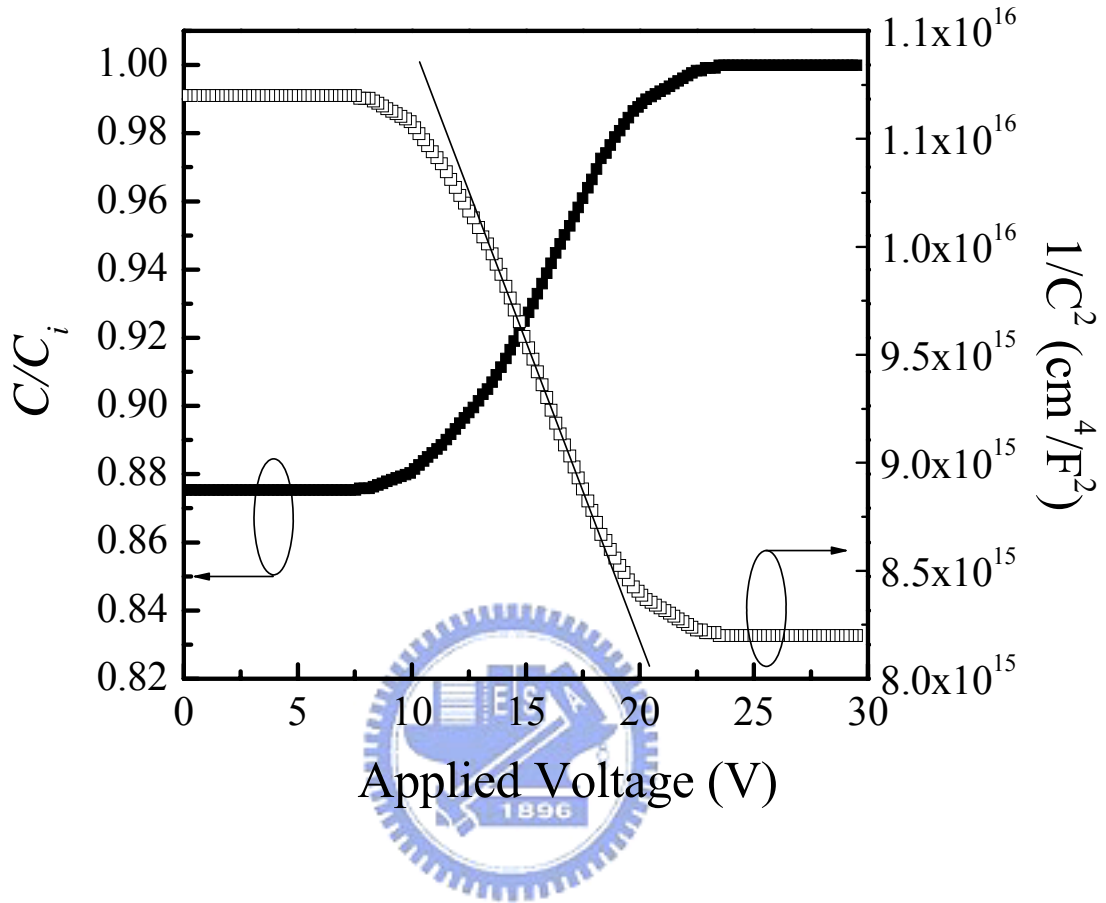Figure 4-13 Transfer characteristics of Zn$_{(1-x)}$Zr$_x$O-TFTs with various Zr content.

Figure 4-14 The capacitance-voltage characteristics and a plot of $1/C^2$ as a function of voltage of Zn$_{(1-x)}$Zr$_x$O MOS structure where x = 0.03.
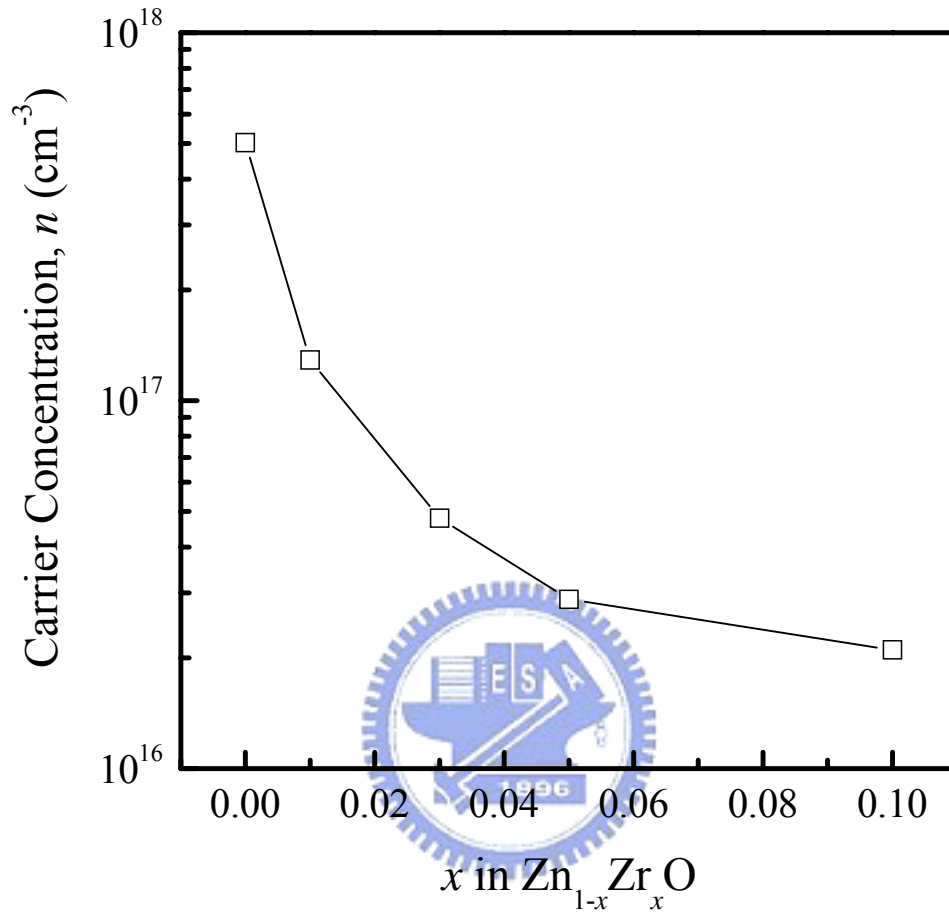
Figure 4-15 Carrier concentration (*n*) of Zn$_{(1-x)}$Zr$_x$O thin films as a function

of the Zr content.

Table 4-1 Electrical performance (saturation mobility μ$_{sat}$, threshold voltage V_{th}, minimum off-current I_{off} and on/off current ratio) of Zn$_{(1-x)}$Zr$_x$O thin-film transistors.

x in Zn$_{(1-x)}$Zr$_x$O	μ$_{sat}$(cm^2/Vs)	V_{th}(V)	I_{off} (A/μm)	I_{on}/I_{off}
0.00	0.40	-31.9	7.20×10^{-7}	<10
0.01	0.34	-9.90	2.86×10^{-11}	1.34×10^5
0.03	0.28	4.72	3.24×10^{-13}	8.89×10^6
0.05	0.10	10.4	2.14×10^{-13}	4.28×10^6
0.10	0.03	20.5	1.28×10^{-13}	1.52×10^6